DISCONTINUOUS GALERKIN METHOD FOR SOLVING 2D DISSIPATIVE SEISMIC WAVE EQUATIONS

XIJUN HE[1], CHUJUN QIU[2] and JIANQIANG SUN[3]

[1] *School of Mathematics and Statistics, Beijing Technology and Business University (BTBU), Beijing 100048, P.R. China. hexijun111@sina.com*
[2] *Department of Mathematical Sciences, Tsinghua University, Beijing 100000, P.R. China.*
[3] *Department of Mathematical Sciences, Hainan University, Haikou 100000, P.R. China.*

(Received July 8, 2021; revised version accepted January 16, 2022)

ABSTRACT

He, X.J., Qui, C.J. and Sun, J.Q., 2022. Discontinuous Galerkin method for solving 2D dissipative seismic wave equations. *Journal of Seismic Exploration*, 31: 153-176.

Seismic dissipation widely exists in underground media. To develop a detailed understanding of wave propagation in dissipative media, in this study, we introduce a discontinuous Galerkin (DG) method for solving acoustic and elastic wave equations in D'Alembert media. This method uses the numerical flux-based DG formulations with the explicit 3rd-order total variation diminishing (TVD) time discretization. We first derive an empirical formula for numerical stability conditions, which shows that the relative error of the Courant-Friedrichs-Lewy (CFL) condition numbers between the actual the numerical cases does not exceed 3%. The analyses also show that both the dispersion and dissipation in D'Alembert media are frequency dependent, and have a strong correlation with the dissipation factor. Finally, we present some numerical experiments. The quantitative comparisons of the attenuation ratios of the waveforms show that they are close to the theoretical ones, verifying the findings of the analyses. In particular, for elastic waves, the relative errors between the numerical attenuation ratios and the theoretical ones do not exceed 4%. The simulation of dissipative elastic wave propagation in a model with surface topography indicates our method is capable of dealing with complex geometry.

KEY WORDS: discontinuous Galerkin method, D'Alembert media, dispersion, dissipation, numerical modelling.

0963-0651/22/$5.00

INTRODUCTION

The underground medium is not completely elastic, and often exhibits dissipation (Niu and Sun, 2007). Therefore, the study of seismic waves in dissipative media is of much value and helpful for understanding the earth. Dissipative properties are usually described by making some modifications to the displacement, stress or strain in seismic wave equations. There are many viscoelastic models such as the Maxwell model, the Kelvin model, the Boltzmann model and the D'Alembert model (Emmerich and Korn, 1987; Carcione and Cavallini, 1994; Aki and Richards, 2002; Moczo and Kristek, 2005; Ba et al., 2017). Among these models, the Maxwell, Kelvin and Boltzmann models are obtained by modifying the stress–strain relations, but the D'Alembert model is obtained by directly adding viscous forces to the dynamic equilibrium equation to describe the influence of the friction.

The D'Alembert model has many imperfections compared with other viscoelastic models. For instance, it has similar viscosity and attenuation properties of *P* wave and *S* wave, but these should have different behaviors in the dispersion and dissipation characteristics. Also, the physical meaning of the viscosity coefficient in the D'Alembert model is not clear. However, the D'Alembert model has many advantages. In terms of the complexity of the equations, the D'Alembert model is the simplest viscoelastic model, and it avoids the problems of complex device combinations that occur in other models such as the Maxwell and Kelvin models. The D'Alembert model is also practical and effective, and contains fewer petrophysical parameters that can macroscopically describe the strong attenuation mechanism in complex media. From the aspect of numerically solving the equations, this can save a lot of computation. Moreover, the other aforementioned viscoelastic models can be transformed into a first-order hyperbolic wave propagation system by adding a dissipative term, which are similar to the D'Alembert model. Therefore, the study of the D'Alembert model is helpful to understand the dispersion and dissipation properties of other viscoelastic models. In these regards, we use the D'Alembert model in this study.

Numerous studies have been carried out to numerically solve the dissipative wave equations. A lot of numerical schemes have emerged, such as finite difference methods (Robertsson et al., 1994; Hestholm, 1999; Kristek and Moczo, 2003; Wang and Zhou, 2014; Wang et al., 2019), finite element methods (Yang and Du, 2003), pseudo-spectral methods (Carcione, 1993), and spectral element methods (Cai et al., 2017). Recently, the discontinuous Galerkin (DG) method for solving wave equations has attracted great attention. Many variants of the DG method have been proposed and applied (e.g., Reed and Hill, 1973; Rivière et al., 2007; Ferroni et al., 2017). Particularly, Cockburn and Shu (1989) propose the Runge-Kutta discontinuous Galerkin (RKDG) method to solve hyperbolic conservation laws, and its variants have been widely used (e.g., Sármány et al., 2007; He et al., 2015).

Compared with traditional numerical methods, the DG method has many advantages in dealing with high-order accuracy, complex structures and boundary conditions. The method also has good parallelism and can effectively suppress the numerical dispersion. In computational geophysics, Käser and Dumbser (2006) proposed an arbitrary high-order derivatives DG (ADER-DG) method, which has been widely used in seismology (Käser et al., 2007; de la Puente et al., 2008). Since then, there has been significant progress in the DG method for solving seismic wave equations (e.g., de Basabe et al., 2008; Etienne et al., 2010; Wilcox et al., 2010; He et al., 2015; Yang et al., 2016; Zhang et al., 2018). Many researches have been devoted to solving the wave equations in viscoelastic media. Käser et al. (2007) employed the ADER-DG method to solve the heterogeneous anelastic seismic wave equations on 3D unstructured tetrahedral meshes, and they used the generalized Maxwell viscoelastic model. Rivière et al. (2007) proposed a symmetric or non-symmetric interior penalty DG method to solve the linear solid viscoelasticity problems. Lähivaara and Huttunen (2010) suggested a discontinuous Galerkin method with non-uniform basis order to solve the 3D dissipative acoustic wave equation. Lambrecht et al. (2018) proposed a nodal discontinuous Galerkin approach for the computation of viscoelastic wavefields.

The dissipative wave equations can be viewed as a wave propagation system by adding a dissipative term. The hyperbolic wave propagation system is non-stiff, but it becomes a stiff system when the dissipative factor is large. These two systems can also be encountered in solving wave propagations in porous media. Among the numerical methods for solving viscoelastic or porous wave equations, many use the splitting method (e.g., Carcione and Quiroga-Goode, 1995; McLachlan and Quispel, 2002; Cai et al., 2017) or the so-called fractional-step method. The splitting method has many advantages, such as the use of large Courant-Friedrichs-Lewy (CFL) condition numbers and fast computational speed. However, as de la Puente et al. (2008) pointed out, this splitting method also has some limitations, for instance, it is difficult to improve the numerical accuracy.

Based on these considerations, in this study we do not use the splitting method, but directly use the classic RKDG method to solve the dissipative wave equations. We use modal basis functions, the local Lax-Friedrichs (LLF) flux, and employs the explicit 3rd-order TVD Runge-Kutta method for time discretization. The novelty of this study lies in the introduction of the DG method to solve dissipative acoustic and elastic wave equations with detailed numerical stability, dispersion and dissipation analyses. These analyses are instructive for the understanding of dissipative seismic wave propagation.

WAVE EQUATIONS IN D'ALEMBERT MEDIA

Acoustic wave equation in D'Alembert media

The vector wave-field in D'Alembert media can be decomposed into a

P wave and a *P-SV* wave fields, where the *P* wave equation in the 2D *x-z* plane has the following form:

$$\rho\frac{\partial^2 u}{\partial t^2}+\eta\frac{\partial u}{\partial t}=\frac{\partial}{\partial x}\left(\mu\frac{\partial u}{\partial x}\right)+\frac{\partial}{\partial z}\left(\mu\frac{\partial u}{\partial z}\right), \tag{1}$$

where u is the pressure field, ρ is the density, μ is the elastic constant. Here η is a viscous parameter that relates to the dissipative property. The term $\eta\partial u/\partial t$ describes the damping force. To transform eq. (1) into a first-order system, we introduce two shear stresses σ_{xy} and σ_{zy} with $\sigma_{xy}=\mu\,\partial u/\partial x$ and $\sigma_{zy}=\mu\,\partial u/\partial z$, then we have:

$$\rho\frac{\partial^2 u}{\partial t^2}+\eta\frac{\partial u}{\partial t}=\frac{\partial}{\partial x}\left(\sigma_{xy}\right)+\frac{\partial}{\partial z}\left(\sigma_{zy}\right). \tag{2}$$

Let $v=\partial u/\partial t$ and $r=\eta/\rho$, then we can rewrite eq. (2) as follows:

$$\begin{cases}\dfrac{\partial v}{\partial t}+rv=\dfrac{1}{\rho}\dfrac{\partial}{\partial x}\left(\sigma_{xy}\right)+\dfrac{1}{\rho}\dfrac{\partial}{\partial z}\left(\sigma_{zy}\right)\\ \dfrac{\partial\sigma_{xy}}{\partial t}=\mu\dfrac{\partial v}{\partial x}\\ \dfrac{\partial\sigma_{zy}}{\partial t}=\mu\dfrac{\partial v}{\partial z}\end{cases}, \tag{3}$$

where r is called the dissipation factor. We have $r = \omega Q^{-1}$, where ω is the dominant frequency of the wavefield and Q is the quality factor of medium. Let:

$$\boldsymbol{W}=\begin{bmatrix}v\\ \sigma_{xy}\\ \sigma_{zy}\end{bmatrix},\quad \boldsymbol{A}_1=\begin{bmatrix}0 & -1/\rho & 0\\ -\mu & 0 & 0\\ 0 & 0 & 0\end{bmatrix},\quad \boldsymbol{A}_2=\begin{bmatrix}0 & 0 & -1/\rho\\ 0 & 0 & 0\\ -\mu & 0 & 0\end{bmatrix},\quad \boldsymbol{B}=\begin{bmatrix}r & 0 & 0\\ 0 & 0 & 0\\ 0 & 0 & 0\end{bmatrix}, \tag{4}$$

then eq. (3) can be transformed into the following first-order system:

$$\frac{\partial\boldsymbol{W}}{\partial t}+A_1\frac{\partial\boldsymbol{W}}{\partial x}+A_2\frac{\partial\boldsymbol{W}}{\partial z}+\boldsymbol{B}\boldsymbol{W}=0 \quad . \tag{5}$$

The matrix $\boldsymbol{B}$ is related to the damping force in D'Alembert media.

Elastic wave equations in D'Alembert media

The 2D source-free *P-SV* wave equations with velocity-stress form in D'Alembert media can be written as:

$$\begin{cases} \dfrac{\partial v}{\partial t} - \dfrac{1}{\rho}\left(\dfrac{\partial \sigma_{xx}}{\partial x} + \dfrac{\partial \sigma_{xz}}{\partial z}\right) + rv = 0 \\ \dfrac{\partial w}{\partial t} - \dfrac{1}{\rho}\left(\dfrac{\partial \sigma_{xz}}{\partial x} + \dfrac{\partial \sigma_{zz}}{\partial z}\right) + rw = 0 \\ \dfrac{\partial \sigma_{xx}}{\partial t} - (\lambda + 2\mu)\dfrac{\partial v}{\partial x} - \lambda \dfrac{\partial w}{\partial z} = 0 \\ \dfrac{\partial \sigma_{xz}}{\partial t} - \mu\left(\dfrac{\partial w}{\partial x} + \dfrac{\partial v}{\partial z}\right) = 0 \\ \dfrac{\partial \sigma_{zz}}{\partial t} - (\lambda + 2\mu)\dfrac{\partial w}{\partial z} - \lambda \dfrac{\partial v}{\partial x} = 0 \end{cases}, \tag{6}$$

where v and w are its components in the x and z directions, respectively. λ and μ are elastic constants. r is called the dissipation factor. Following the deformation of the acoustic equation, we introduce the vector: $\boldsymbol{W} = \left(v, w, \sigma_{xx}, \sigma_{xz}, \sigma_{zz}\right)^T$, and define the matrices $\boldsymbol{A}_1$, $\boldsymbol{A}_2$, and $\boldsymbol{B}$ as follows:

$$\boldsymbol{A}_1 = \begin{pmatrix} 0 & 0 & -1/\rho & 0 & 0 \\ 0 & 0 & 0 & -1/\rho & 0 \\ -(\lambda+2\mu) & 0 & 0 & 0 & 0 \\ 0 & -\mu & 0 & 0 & 0 \\ -\lambda & 0 & 0 & 0 & 0 \end{pmatrix}, \quad \boldsymbol{A}_2 = \begin{pmatrix} 0 & 0 & 0 & -1/\rho & 0 \\ 0 & 0 & 0 & 0 & -1/\rho \\ 0 & -\lambda & 0 & 0 & 0 \\ -\mu & 0 & 0 & 0 & 0 \\ 0 & -(\lambda+2\mu) & 0 & 0 & 0 \end{pmatrix}, \tag{7}$$

$$\boldsymbol{B} = \begin{pmatrix} r & 0 & 0 & 0 & 0 \\ 0 & r & 0 & 0 & 0 \\ 0 & 0 & 0 & 0 & 0 \\ 0 & 0 & 0 & 0 & 0 \\ 0 & 0 & 0 & 0 & 0 \end{pmatrix}, \tag{8}$$

then eq. (6) can be written in the form of system (5).

DISCONTINUOUS GALERKIN METHOD

Spatial discretization

We now construct the DG method for solving eq. (5). Assuming that $\Omega \subseteq \mathbf{R}^2$ is a bounded domain, which is divided into non-overlapping elements with $\Omega = \bigcup_i \Omega_i$. We then define the approximation test function space as $V_h = \left\{ v \in L^2(\Omega) : v\big|_{\Omega_i} \in P^\kappa(\Omega_i) \right\}$. Here, $P^\kappa(\Omega_i)$ denotes the space of polynomials of degree less than or equal to κ defined on Ω_i. We need to determine a set of scalar basis functions for the space V_h. There are nodal and modal basis functions, such as Legendre polynomials and Lagrange basis functions based on Gauss quadrature points. Here, for simplicty, we use the modal basis functions and take monomial functions $\left\{ x^\alpha z^\beta \mid 0 \le \alpha + \beta \le \kappa \right\}$ for both quadrilateral and triangular elements. Also, we assume that the coefficients matrices $\boldsymbol{A}_1$, $\boldsymbol{A}_2$, and $\boldsymbol{B}$ to be piecewise constant in each element. We define $\boldsymbol{F}(\boldsymbol{W}) = (\boldsymbol{A}_1\boldsymbol{W}, \boldsymbol{A}_2\boldsymbol{W})$ and $\nabla = (\partial_x, \partial_z)$, then eq. (5) can be written as:

$$\frac{\partial \boldsymbol{W}}{\partial t} + \nabla \cdot \boldsymbol{F}(\boldsymbol{W}) + \boldsymbol{B}\boldsymbol{W} = 0 \quad . \tag{9}$$

Multiplying eq. (9) by a scalar test function v and integrating on Ω_i, using Green's formula, we obtain the following weak form:

$$\int_{\Omega_i} \left(v \frac{\partial \boldsymbol{W}}{\partial t} + v\boldsymbol{B}\boldsymbol{W} - \boldsymbol{F}(\boldsymbol{W}) \cdot \nabla v \right) dV + \int_{\partial\Omega_i} v\boldsymbol{F}(\boldsymbol{W}) \cdot \boldsymbol{n} \, dS = 0 \quad , \tag{10}$$

where $\boldsymbol{n} = (n_1, n_2)^T$ is the outward unit normal vector. Since the test function space is locally defined, it allows the approximate solution $\boldsymbol{W}$ to be discontinuous at the interior interface $\partial\Omega_i$. We let $\boldsymbol{W}^{\text{int}}$ and $\boldsymbol{W}^{\text{ext}}$ denote the approximate solutions of $\boldsymbol{W}$ from the interior and exterior of $\partial\Omega_i$, respectively, then we can use the numerical flux $\hat{\boldsymbol{F}}(\boldsymbol{W}^{\text{int}}, \boldsymbol{W}^{\text{ext}}, \boldsymbol{n})$ to replace $\boldsymbol{F}(\boldsymbol{W}) \cdot \boldsymbol{n}$. The compatibility and conservation conditions must be satisfied for the numerical flux between two adjacent elements. Here we use the simple and commonly used LLF flux (Cockburn and Shu, 1989), which is:

$$\hat{\boldsymbol{F}}(\boldsymbol{W}^{\text{int}}, \boldsymbol{W}^{\text{ext}}, \boldsymbol{n}) = \frac{1}{2}\left[\boldsymbol{F}(\boldsymbol{W}^{\text{int}}) + \boldsymbol{F}(\boldsymbol{W}^{\text{ext}}) \right] \cdot \boldsymbol{n} - \frac{\upsilon}{2}(\boldsymbol{W}^{\text{int}} - \boldsymbol{W}^{\text{ext}}), \tag{11}$$

where υ is the numerical viscosity constant that can be evaluated as the largest eigenvalue (in absolute value) of $\partial(\boldsymbol{F}(\boldsymbol{W}^{\text{int}})\cdot\boldsymbol{n})/\partial\boldsymbol{W}$ and $\partial(\boldsymbol{F}(\boldsymbol{W}^{\text{ext}})\cdot\boldsymbol{n})/\partial\boldsymbol{W}$. To load the free surface boundary conditions, we can take an exterior velocity that is identical to the interior one, and impose an opposite stress wavefield. As a result, we can keep a continuous velocity and a zero stress on the free surface (Etienne et al., 2010). For the absorbing boundary condition, we simply take $\boldsymbol{W}^{\text{ext}}=0$ (Käser and Dumbser, 2006).

Next, we let $\left\{w_l^i\right\}_{l=0}^{l=N-1}$ denote the basis functions series, then we have the basis function expansions $\boldsymbol{W}\big|_{\Omega_i}=\sum_{l=0}^{N-1}\boldsymbol{C}_l^i(t)w_l^i$, where $\left\{C_l^i(t)\right\}_{l=0}^{N-1}$ are the time-dependent coefficients. Substituting the expansions of $\boldsymbol{W}$ into eq. (10) and considering the numerical flux, we obtain the following equations for DG spatial discretization:

$$\sum_{l=0}^{N-1}\frac{\partial\boldsymbol{C}_l^i(t)}{\partial t}\int_{\Omega_i}w_l^iw_{l'}^i dV+\sum_{l=0}^{N-1}\boldsymbol{B}\boldsymbol{C}_l^i(t)\int_{\Omega_i}w_l^iw_{l'}^i dV-\int_{\Omega_i}\boldsymbol{F}\left(\sum_{l=0}^{N-1}\boldsymbol{C}_l^i(t)w_l^i\right)\cdot\left(\frac{\partial w_{l'}^i}{\partial x},\frac{\partial w_{l'}^i}{\partial z}\right)dV$$
$$+\sum_j\int_{\Omega_i\cap\Omega_j}w_{l'}^i\hat{\boldsymbol{F}}\left(\sum_{l=0}^{N-1}\boldsymbol{C}_l^i(t)w_l^i,\sum_{l=0}^{N-1}\boldsymbol{C}_l^j(t)w_l^j,\boldsymbol{n}\right)dS=0\qquad l'=0,\ldots,N-1 \tag{12}$$

where Ω_j is the adjacent element which shares a common edge with Ω_i.

Time discretization

The next step is to solve the semi-discrete system (12). For simplicity of notations, we introduce a vector $\boldsymbol{C}(t)$ to represent all the coefficients in the domain, and we use a linear operator *L* to cover the spatial discretization in eq. (12), then we can write the ordinary differential equations (ODEs) as:

$$\frac{\partial\boldsymbol{C}}{\partial t}=L(\boldsymbol{C}) \tag{13}$$

To simplify the discussions, we assume that the operator *L* does not

depend on t. There are numerous time integration methods to solve eq. (13), such as explicit Runge-Kutta methods, the arbitrary high-order derivatives (ADER) time stepping method (Dumbser and Käser, 2006) and a lot of implicit techniques. Here, we employ the explicit 3rd-order TVD Runge-Kutta method (Cockburn and Shu, 1989), which is:

$$\begin{cases} \boldsymbol{C}^{(0)} = \boldsymbol{C}^{(n)} \\ \boldsymbol{C}^{(1)} = \boldsymbol{C}^{(0)} + \Delta t L(\boldsymbol{C}^{(0)}) \\ \boldsymbol{C}^{(2)} = \frac{3}{4}\boldsymbol{C}^{(0)} + \frac{1}{4}\boldsymbol{C}^{(1)} + \frac{1}{4}\Delta t L(\boldsymbol{C}^{(1)}) \\ \boldsymbol{C}^{(n+1)} = \frac{1}{3}\boldsymbol{C}^{(0)} + \frac{2}{3}\boldsymbol{C}^{(2)} + \frac{2}{3}\Delta t L(\boldsymbol{C}^{(2)}) \end{cases} . \tag{14}$$

STABILITY, DISPERSION AND DISSIPATION ANALYSES

In this section, we present the numerical analysis of the DG method for solving dissipative acoustic wave equations in D'Alembert media. We first assume that the domain is unbounded and source-free. These assumptions are commonly used (e.g., Hu et al., 1999; de Basabe et al., 2008; Ferroni et al., 2017). Then, the domain is discretized uniformly by quadrilateral elements (Fig. 1), in which the typical element is denoted by E^{nm}. The spatial steps in the x and z directions are assumed to be h. Then, the DG spatial discretization in eq. (12) can be written as (Hu et al., 1999):

$$\boldsymbol{Q}\frac{\partial \boldsymbol{C}^{nm}}{\partial t} = \boldsymbol{N}_0\boldsymbol{C}^{nm} + \boldsymbol{N}_{-1}\boldsymbol{C}^{n-1m} + \boldsymbol{N}_{+1}\boldsymbol{C}^{n+1m} + \boldsymbol{M}_0\boldsymbol{C}^{nm} + \boldsymbol{M}_{-1}\boldsymbol{C}^{nm-1} + \boldsymbol{M}_{+1}\boldsymbol{C}^{nm+1} + \boldsymbol{H}\boldsymbol{C}^{nm}, \tag{15}$$

where $\boldsymbol{C}^{nm}$ is the vector that contains all the coefficients in E^{nm}. The explicit expressions of these matrices are shown in Hu et al. (1999) and He et al. (2015). To perform the analysis, we assume the solution is a plane wave $\boldsymbol{C}^{nm} = \boldsymbol{C}\exp[\mathrm{i}(k\cos\theta nh + k\sin\theta mh)]$, where k is the wave number and θ is the propagation angle. Substituting it into eq. (15) gives:

$$\frac{\partial \boldsymbol{C}}{\partial t} = \boldsymbol{Q}^{-1}\left[\boldsymbol{N}_0 + \boldsymbol{N}_{-1}\mathrm{e}^{-\mathrm{i}k\cos\theta h} + \boldsymbol{N}_{+1}\mathrm{e}^{\mathrm{i}k\cos\theta h} + \boldsymbol{M}_0 + \boldsymbol{M}_{-1}\mathrm{e}^{-\mathrm{i}k\sin\theta h} + \boldsymbol{M}_{+1}\mathrm{e}^{\mathrm{i}k\sin\theta h} + \boldsymbol{H}\right]\boldsymbol{C}. \tag{16}$$

Then we can use the explicit 3rd-order TVD Runge-Kutta method introduced above to solve eq. (16)

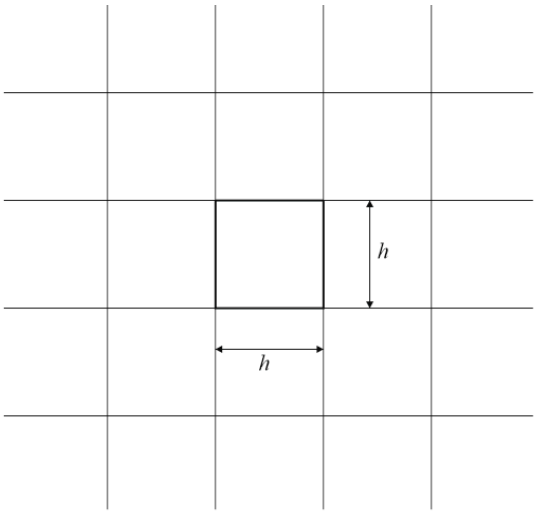

Fig. 1. Illustration of the discretized rectangular elements.

Stability conditions

We now consider the stability for the numerical algorithm. To keep the scheme stable, the time step, spatial step and the acoustic wave speed are required to satisfy $\Delta t \le \alpha_{\max} h/V_P$, where $\alpha_{\max}$ is the Courant-Friedrichs-Lewy (CFL) condition number or the so-called maximum Courant number and $V_P = \sqrt{\mu/\rho}$ is the acoustic velocity. Let Λ be the maximal modulus of the eigenvalues of the growing matrix [the matrices on the right side of eq. (16)], then solving $|\Lambda| \le 1$ for $kh \in [0, \pi]$ and $\theta \in [0, 2\pi]$, we can obtain the CFL condition numbers $\alpha_{\max}$ for the scheme.

Instead of computing $\alpha_{\max}$ as indicated above, in what follows we will discuss an empirical formula to evaluate the CFL condition numbers. We first notice that the semi-discrete system (12) can be divided into two parts, one is hyperbolic without dissipation, and the other is dissipative. Therefore, accordingly, we can divide the ODE system (13) into two parts, which can be written as (Carcione and Quiroga-Goode, 1995):

$$\frac{\partial \boldsymbol{C}}{\partial t} = L(\boldsymbol{C}) = L_1(\boldsymbol{C}) + L_2(\boldsymbol{C}). \tag{17}$$

The operator L_1 is related to the wave propagation without dissipation, and L_2 is related to the dissipation. We want to find the maximal eigenvalues (in absolute value) of operators L_1 and L_2, denoted by λ_1 and λ_2,

respectively. For the hyperbolic system:

$$\frac{\partial \boldsymbol{C}}{\partial t} = L_1(\boldsymbol{C}), \tag{18}$$

the CFL condition has been analyzed based on the plane-wave analysis method (He et al., 2015). For ithe DG method equipped with quadratic basis function (κ = 2), LLF flux and 3rd-order TVD Runge-Kutta time discretization, we have the following stability result for the quadrilateral elements in Fig. 1:

$$\Delta t \le \alpha_{\max} \frac{h}{V_P} \approx 0.164 \frac{h}{V_P}. \tag{19}$$

In addition, based on the numerical analysis theory of solving the ODE system by using the explicit 3rd-order Runge-Kutta method (Li et al., 2008), we have $\Delta t \le 2.51/\lambda_1$. Then, λ_1 can be evaluated as $\lambda_1 \approx \frac{2.51 V_P}{0.164h}$.

For the dissipative system:

$$\frac{\partial \boldsymbol{C}}{\partial t} = L_2(\boldsymbol{C}) \quad . \tag{20}$$

Since L_2 is only related to the matrix $\boldsymbol{B}$, the largest eigenvalue (in absolute value) for the operator L_2 is $\lambda_2 \approx r$, where r is the dissipation factor in eq. (3).

Let λ be the largest eigenvalue (in absolute value) for the operator L, since $L(\boldsymbol{C}) = L_1(\boldsymbol{C}) + L_2(\boldsymbol{C})$, then we have $\lambda \le \lambda_1 + \lambda_2$. Using the explicit 3rd-order Runge-Kutta time discretization, taking the time step $\Delta t \le 2.51/(\lambda_1 + \lambda_2) \le 2.51/\lambda$, we get a stable scheme. Thus, we obtain an empirical formula for the CFL condition:

$$\Delta t \le \frac{2.51}{\frac{2.51 V_P}{0.164h} + r}, \quad \text{or} \quad \frac{V_P \Delta t}{h} \le \alpha'_{\max} \approx \frac{2.51 V_P}{\frac{2.51 V_P}{0.164} + hr}. \tag{21}$$

In practical applications, we find that eq. (21) are reasonable estimates. Table 1 lists the comparisons between the actual CFL condition numbers $\alpha_{\max}$ and the numbers $\alpha'_{\max}$ obtained from the empirical equations for some

cases. From the table, we see that the difference between $\alpha_{\max}$ and $\alpha'_{\max}$ is small, and the relative error does not exceed 3%. It is also observed that as the dissipation factor r increases, the time step decreases. When the dissipation factor r is large enough, the system is stiff and the time step would be very small.

Table 1. A comparison of the actual CFL condition numbers $\alpha_{\max}$ and the numbers $\alpha'_{\max}$.

V_P = 1 km/s, h = 0.01 km			V_P = 1 km/s, r = 100		
r	$\alpha_{\max}$	$\alpha'_{\max}$	h	$\alpha_{\max}$	$\alpha'_{\max}$
10	0.164	0.1629	0.1	0.099	0.0992
100	0.156	0.1539	0.05	0.124	0.1236
1000	0.099	0.0992	0.02	0.146	0.1450
10000	0.021	0.0217	0.01	0.156	0.1539

For a triangular mesh, we apply a heuristic stability criterion that works well from numerical tests (He et al., 2015): $\Delta t \le \alpha'_{\max} \min(h_{\min}/V_P)/2$, where $h_{\min}$ is the shortest edge of the triangular element. Note that the criterion is empirical and we currently have no theoretical deduction about it.

Dispersion-dissipation analysis

We now study the dispersion-dissipation properties of the scheme. The derivation follows studies by Hu et al. (1999), de Basabe et al. (2008) and He et al. (2015). We are not going to repeat the derivation step by step, but just show some key points. We assume that $\boldsymbol{C}^{(n)} = \boldsymbol{C}^0 \mathrm{e}^{-\mathrm{i}\omega n\Delta t}$, where ω is the angular frequency. We decompose ω with $\omega = \omega_r - \mathrm{i}\omega_i$, where ω_r and ω_i are related to the numerical dispersion and dissipation, respectively. The numerical acoustic wave speed is computed by $V_{num} = \omega_r/k$. We define the dispersion as $R = V_{num}/V_P = \omega_r \Delta t/(\alpha kh)$, where the Courant number α is defined as $\alpha = c\,\Delta t/h$.

Figs. 2 and 3 show the dispersion. We set the parameters V_P = 4 km/s, r = 10, h = 0.05 km, and $\alpha = c\,\Delta t/h = 0.1$. Fig. 2a shows R as a function of the frequency. In our analysis, ω is a complex number, therefore, we use the

modulus $|\omega|$ to represent the frequency. Fig. 2b is an enlarged view of Fig. 2a. The blue line in Fig. 2 represents the exact dispersion curve which is calculated by (Niu and Sun, 2007):

$$R = \sqrt{2 \Big/ \left(\sqrt{1 + (\frac{r}{|\omega|})^2} + 1 \right)}. \tag{22}$$

The curves in other colors in Fig. 2 indicate different propagation directions, from which we see the obvious anisotropy of the numerical dispersion errors. It is also seen that at low frequencies, R is less than 1, which indicates that the existence of the viscous term causes the wave delay effect; as the frequency increases, R approaches to 1; as the frequency continues to increase, the deviation between the numerical wave velocity V_{num} and V_p begins to increase again. Consequently, we conclude that the dispersion can be divided into two stages. The dispersion at low frequencies is mainly caused by the viscous term in D'Alembert media. As the frequency increases, the dispersion caused by the dissipation factor becomes smaller, and the numerical dispersion caused by the numerical algorithm dominates. In Fig. 3, we show the numerical dispersion with dissipation factors r = 0 and 10. It can be seen in Fig. 3 that as r increases, the dispersion caused by the dissipation factor becomes more serious, but the numerical dispersion caused by the numerical algorithm changes little.

In Figs. 4 and 5, we show the dissipation $e^{-\omega_i \Delta t}$, which indicates the damping coefficient of the wave amplitude over a time step Δt. The parameters we use are the same as those in Fig. 2.

The blue curve shows the exact dissipation calculated by $e^{-\frac{|\omega|\Delta t}{2}\sqrt{2\sqrt{1+(\frac{r}{|\omega|})^2}-2}}$ (Niu and Sun, 2007).

It is evident that

$$e^{-\frac{|\omega|\Delta t}{2}\sqrt{2\sqrt{1+(\frac{r}{|\omega|})^2}-2}} \approx e^{-\frac{r\Delta t}{2}}, \quad \text{when } r = |\omega|. \tag{23}$$

From Fig. 4 we notice that as $|\omega|$ increases, the limit of the dissipative curve approaches to $e^{-r\Delta t/2} \approx 0.9938$. The curves in other colors in Fig. 4 indicate the numerical dissipation in different propagation directions. Similarly, the numerical dissipation anisotropy can be clearly identified. The

numerical dissipation curve can also be divided into two stages. At low frequencies, the dissipation caused by the existence of the viscous term in D'Alembert media is dominant. At high frequencies, in addition to a step jump decrease, the dissipation has a dominant component caused by the DG discretized method. In Fig. 5, we plot the numerical dissipation with kh for dissipation factors $r = 0$ and 10. It is evident that as the dissipation factor r increases, the dissipation becomes larger.

Next, we show the dispersion and dissipation errors with respect to the sampling points per wavelength G in Fig. 6. G is computed as $G = 2\pi/(kh)$. We define the dispersion error as $E_R = |R\text{-}1|$, and the dissipation error as $E_S = |e^{-\omega_i \Delta t}\text{-}1|$. It is found that to satisfy the dispersion within the criterion $E_R < 0.01$, the points per wavelength would be $G \geq 2.3$ for our method. To reduce the dispersion error to $E_R < 0.001$, it is necessary that $G \geq 3.7$. For the dissipation error, a criterion of $E_S < 0.01$ requires that $G \geq 2.6$; a smaller criterion of $E_S < 0.001$ requires that $G \geq 3.9$.

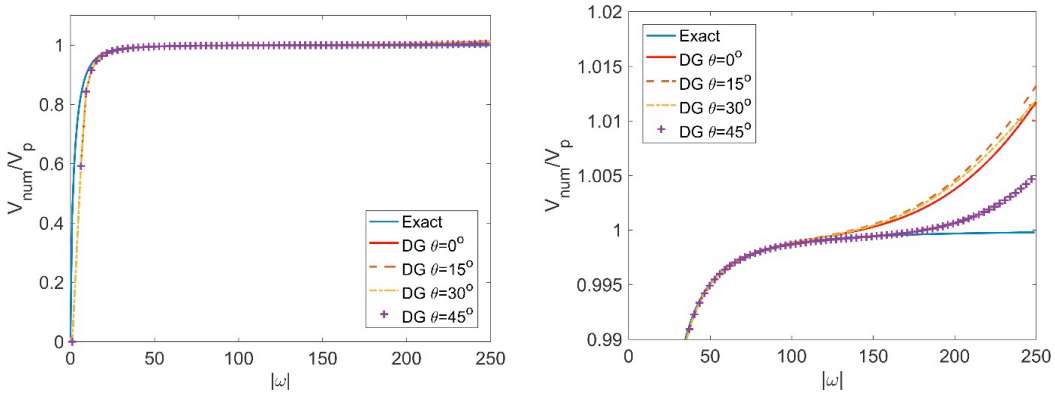

Fig. 2. Dispersion versus frequency, in which (b) is an enlarged version of (a). The blue line shows the exact dispersion, and the other lines show the dispersion in different propagation directions.

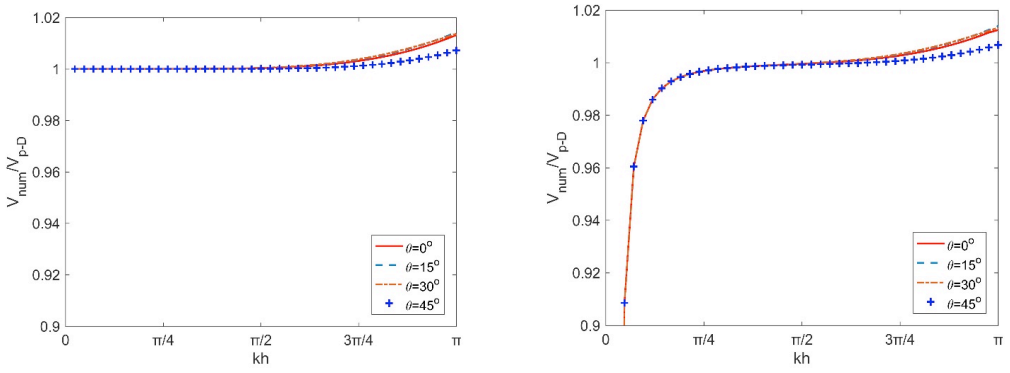

Fig. 3. Dispersion for dissipation factors (a) $r = 0$ and (b) $r = 10$.

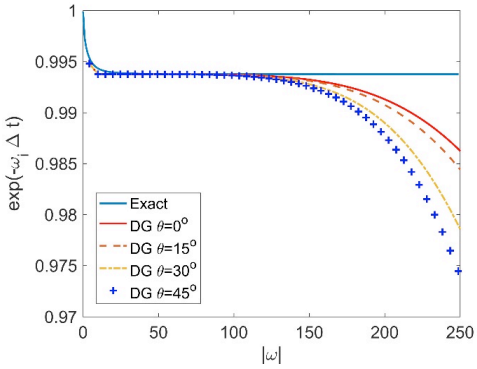

Fig. 4. Dissipation versus frequency. The blue line shows the theoretical dissipation, and the other colored lines show the dissipation in different directions.

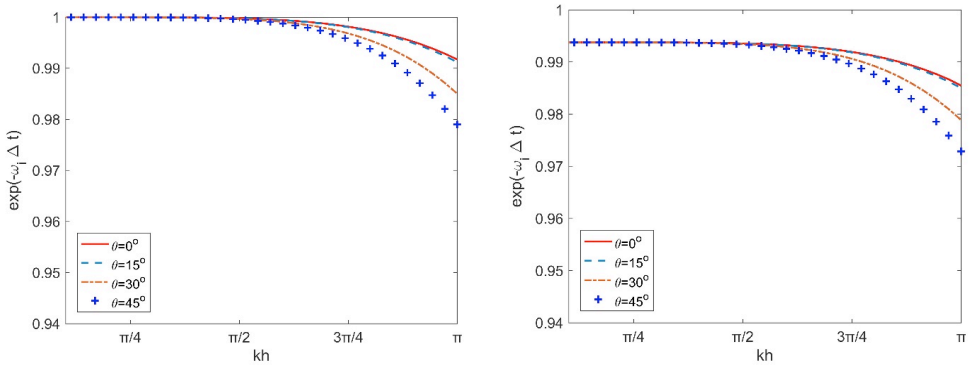

(a) (b)

Fig. 5. Dissipation for dissipation factors (a) $r = 0$ and (b) $r = 10$.

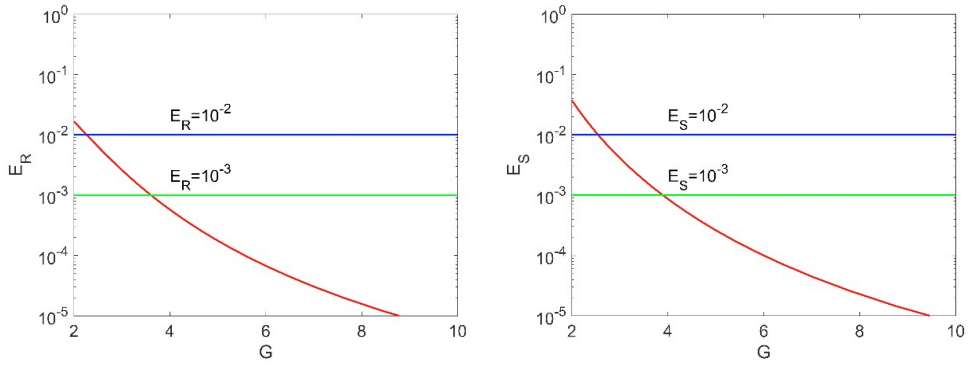

(a) (b)

Fig. 6. Points per wavelength G versus the (a) dispersion error E_R and the (b) dissipation error E_S.

WAVEFIELD SIMULATIONS

In this section, we present several numerical examples to verify the attenuation effect in D'Alembert media. The effect mainly refers to the decay of wave amplitude due to attenuation. The effectiveness of the DG method for solving dissipative wave propagations is also demonstrated. Since the CFL condition number of the DG method decreases significantly with the increase of the basis function, we only consider the quadratic spatial interpolations in this section.

The convergence test

We first consider a model with analytical solutions to verify the convergence of the method. Consider eq. (3) with the following analytical solution:

$$v_{ex}(t,x,z) = e^{-at/2}\cos\left(\frac{2\pi f_0}{c}\cos\theta_0 x + \frac{2\pi f_0}{c}\sin\theta_0 z - Kt\right), \tag{24}$$

where $c = 4$ km/s is the velocity, $\theta_0 = \pi/4$ is the incident angle at time $t = 0$, f_0 is the frequency, and $K = \sqrt{4\pi^2 f_0^2 - r^2/4}$. We take eq. (24) with $t = 0$ as the initial conditions and use the periodic boundary conditions. The computational region is $0 \le x, z \le \sqrt{2}$ km with a homogeneous discretization of square elements in Fig. 1. The time step is 0.0001s, so that the numerical error caused by the time discretization can be ignored. The simulation lasted for 1000 time steps. We define the L^2 error as:

$$E_{L^2} = \left\| v - v_{ex} \right\|_{L^2} = \left(\int_\Omega \left| v - v_{ex} \right|^2 d\Omega \right)^{\frac{1}{2}}. \tag{25}$$

The L^2 errors and convergence orders are listed in Table 2. We see that the numerical error decreases with the reduction of the spatial step, indicating that the DG method is convergent. Since we use quadratic basis functions, the expected 3rd-order of accuracy is obtained. We also see that as the dissipation factor r increases, the magnitude of the error decreases, verifying the attenuation effect in D'Alembert media.

In order to show the problem more clearly, we set a receiver at the center of the domain. Fig. 7 shows the waveforms recorded by the receiver for $f_0 = 8$ Hz and 20 Hz. We observe the obvious decrease in the amplitude as the dissipation factor r increases. In addition, the movement of the trough can be clearly observed from Fig. 7a, but it is not obvious in Fig. 7b. This indicates that the dispersion in D'Alembert media decreases with increasing frequency. We also find that as the dissipation factor r increases, the dispersion in D'Alembert media increases. These observations are consistent with the dispersion and dissipation analyses.

Table 2. Convergence rates of v for the acoustic wave in D'Alembert media.

h (km)	L^2 error	order	L^2 error	order
	$r = 4$ $f_0 = 8$ Hz		$r = 20$ $f_0 = 8$ Hz	
3.536E-02	4.717E-04	-	2.104E-04	-
2.828E-02	2.415E-04	3.00	1.078E-04	3.00
2.357E-02	1.408E-04	2.96	6.295E-05	2.95
2.020E-02	9.057E-05	2.86	4.051E-05	2.86
	$r = 4$ $f_0 = 20$ Hz		$r = 20$ $f_0 = 20$ Hz	
3.536E-02	9.278E-03	-	3.536E-02	-
2.828E-02	4.250E-03	3.50	2.828E-02	3.50
2.357E-02	2.330E-03	3.30	2.357E-02	3.30
2.020E-02	1.426E-03	3.18	2.020E-02	3.18

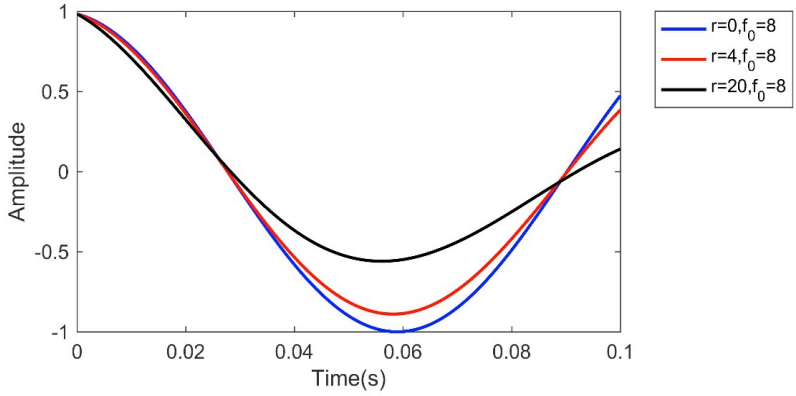

(a)

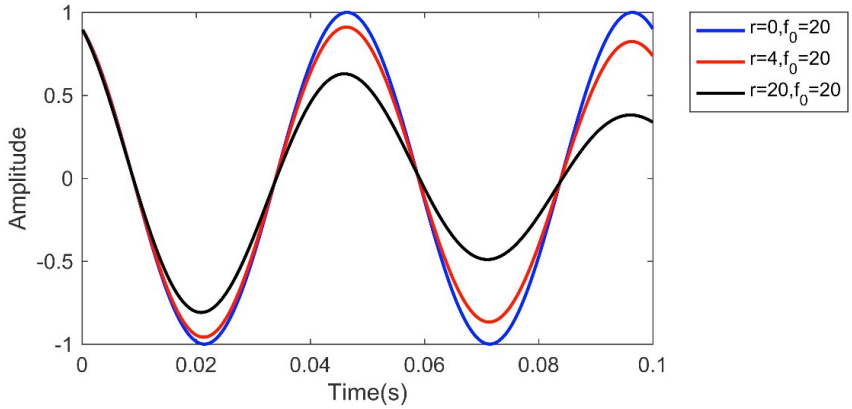

(b)

Fig. 7. Waveforms at the receiver with (a) $f_0 = 8$ and (b) $f_0 = 20$.

Acoustic wave model in D'Alembert media

In the second example, we study the homogeneous acoustic wave propagation with a point source. We consider a square domain with $0 \le x, z \le 10$ km. We discretize the domain with homogeneous square elements as in Fig. 1. V_P = 4 km/s is used. The spatial step is h = 0.05 km, and r = 0, 4, 8, and 16. According to eq. (21), the maximum time step is obtained when r = 0 with Δt = 2.05 ms; the minimum time step is Δt = 2.02 ms when r = 16. Since the difference between the time steps does not exceed 0.1 ms, for convenience, we use Δt = 2 ms for all dissipation factors. The source in this example is a Ricker wavelet with

$$f(t) = -9.6 f_0 (0.6 f_0 t - 1) \exp[-8(0.6 f_0 t - 1)^2]. \quad (26)$$

The central frequency f_0 = 20 Hz is used. The source is located at (5, 5) km. A receiver to detect the waveforms is set at R1 (6.2, 6.2) km.

The waveforms recorded at the receiver are shown in Fig. 8. The numerical solution has a good agreement with the analytical solution with r = 0, which is computed by the Cagnidard-de Hoop method (De Hoop, 1960). It can be observed that with the increase of the dissipation factor r, the amplitudes become significantly smaller, demonstrating the attenuation effect in D'Alembert media. To study this attenuation effect more quantitatively, we record the amplitudes at the crest and trough for r = 4, 8, and 16, and divide them accordingly by the amplitudes at the crest and trough when r = 0. The results are the attenuation ratios of the amplitude. Table 3 lists the amplitudes at the crest and trough recorded in Fig. 8 and their corresponding amplitude attenuation ratios. Also listed are the theoretical attenuation ratios for comparisons, which are given by $e^{-rT/2}$ (see eq. (23)). T is the propagation time for the acoustic wave to travel from the source to the receiver. Here it is easy to calculate: $T = L/V_P = 0.4243$ s. From Table 3 we see the attenuation ratios at the crest and trough are in good agreement with the theoretical cases, which illustrates the correctness of the previous dissipation analysis. In Fig. 9, we also show the snapshots of the wave fields for r = 0 and r = 8 at T = 1.0 s, and the attenuation effect can be clearly observed.

Table 3. The amplitudes and attenuation ratios at the crest and trough.

r	amplitude at crest	amplitude at trough	attenuation ratio at crest	attenuation ratio at trough	theoretical attenuation ratio
0	6.3329E-01	1.0000E+00			
4	2.7100E-01	-4.2768E-01	0.428	0.428	0.428
8	1.1954E-01	-1.8156E-01	0.189	0.182	0.183
16	2.5381E-02	-3.2492E-02	0.040	0.032	0.034

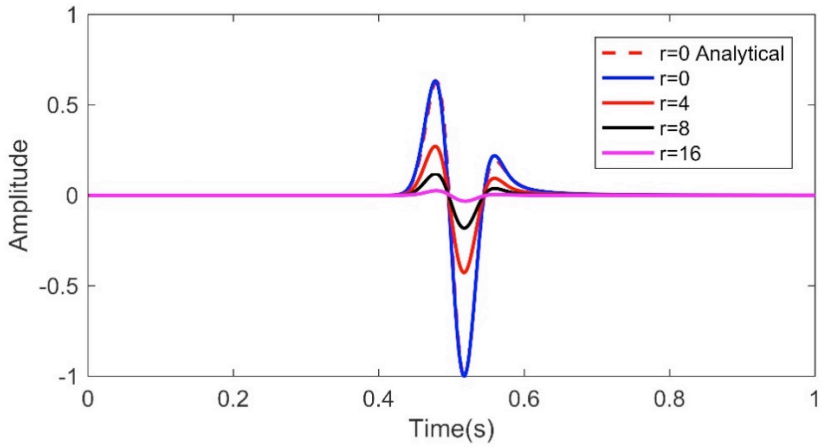

Fig. 8. Waveforms recorded at the receiver with different dissipation factors.

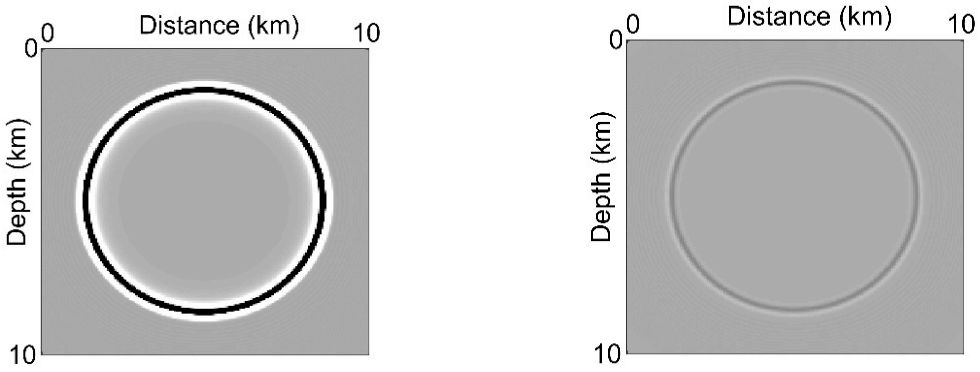

(a) (b)

Fig. 9. Snapshots of the acoustic wave fields for dissipation factors of (a) $r = 2$, (b) $r = 8$.

Elastic wave model in D'Alembert media

In this example, we consider the *P-SV* wave propagation in D'Alembert media. The *P* and *SV* wave velocities are $c_p = 2$ km/s and $c_s = 1.25$ km/s. The density is $\rho = 2$ g/cm^3. The domain is $0 \le x, z \le 2$ km with a homogeneous triangular mesh. The average edge length for the triangles is 20 m. The source is applied in the *z*-direction, and is located at the center of the domain with the source function as in eq. (26) with $f_0 = 20$ Hz. A receiver at (1.3, 1.2) km is set to record the waveforms.

We first consider the case when the dissipation factor $r = 0$. Fig. 10 shows the waveforms for the *v* and *w* components at the receiver. For the purpose of comparison, this model is also simulated by the popular fourth-order finite-difference staggered grid (SG) method (Virieux, 1986; Moczo et al., 2000) with the same computational parameters. The SG method is favored for its easy implementation and low storage requirement.

It is observed that when the spatial step is 20 m, the waveforms of the SG method have evident pseudo fluctuations, demonstrating that the SG method suffers from serious dispersion on coarse mesh. To eliminate the numerical dispersion and offer a reference solution, we perform the simulation with the SG method using a finer grid with a spatial step of 5 m. With the finer grids the SG method produces almost the same solution as that of the DG method on coarse mesh.

We now compare the waveforms with different dissipation factors. Fig.11 shows the waveforms with r = 0, 2, 4 and 8. The attenuation of the amplitude is obviously observed. Table 4 lists the numerical and theoretical numerical attenuation ratios of the *P* and *SV* waves at the crest and trough. We notice that the numerical attenuation ratios at the crest and trough are close to the theoretical ones. For the *P* wave, the relative error does not exceed 2%. For the *SV* wave, the difference between the two does not exceed 4%.

Table 4. The amplitudes and attenuation ratios at the crest and trough for the *P*-*SV* waves.

	r	amplitude at crest	amplitude at trough	attenuation ratio at crest	attenuation ratio at trough	theoretical attenuation ratio
P	0	3.8981E-01	-4.7282E-01			
	2	3.2217E-01	-4.0062E-01	0.826	0.847	0.835
	4	2.6730E-01	-3.3807E-01	0.686	0.715	0.697
	8	1.8595E-01	-2.3871E-01	0.477	0.505	0.486
SV	0	1.0000E+00	-7.1561E-01			
	2	7.5393E-01	-5.3209E-01	0.754	0.744	0.749
	4	5.6761E-01	-3.9744E-01	0.568	0.555	0.562
	8	3.1984E-01	-2.2452E-01	0.320	0.314	0.315

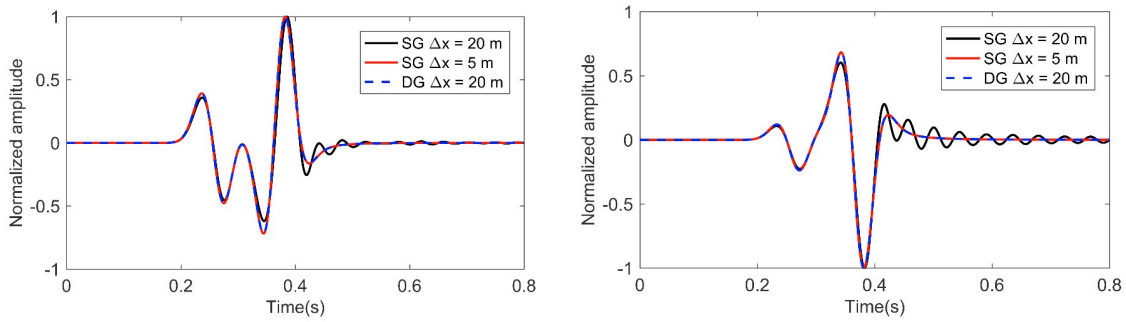

(a) (b)

Fig. 10. Comparisons of the waveforms at the receiver for the DG method and the finite-difference SG method with dissipation factor r = 0. (a) v component and (b) w component.

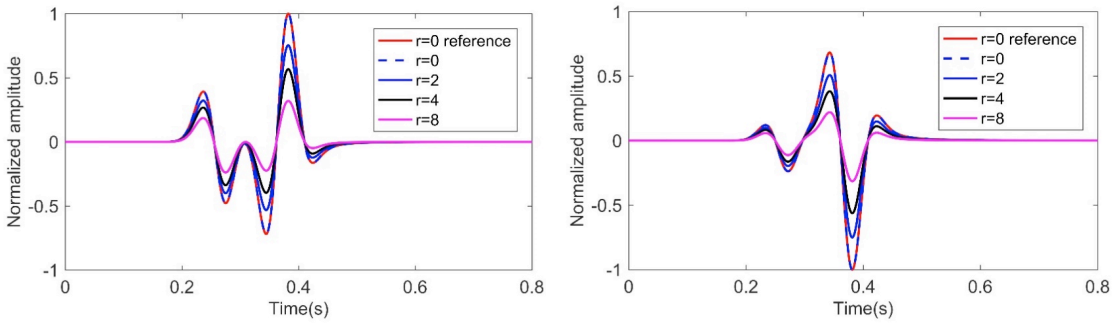

(a) (b)

Fig. 11. Waveforms recorded at the receiver for the velocity components (a) v and (b) w with $r = 0$, 2, 4, and 8. The reference solution for $r = 0$ is computed by the SG method on fine grids.

Lamb's model in D'Alembert media

Here, we test the proposed method for the classical Lamb's problem (Lamb, 1904). The P and SV wave velocities are c_p = 3.2 km/s and c_s = 1.8475 km/s. The density is ρ = 2.2 g/cm^3. The model has a total length of 4 km, the left boundary is at 2 km, and the upper boundary is a slope with a tilt angle $\theta = 10^o$ to test the free surface boundary conditions. The source in this example is a Ricker wavelet with

$$f(t) = \left(t - t_0\right)\exp\left(-(\pi f_0(t - t_0))^2\right) \quad . \tag{27}$$

A central frequency of f_0 = 10 Hz is used. t_0 = 0.08 s is the source decay time. We set the source in both x- and z- directions, with

$$(f_x, f_z) = (-\sin\theta, \cos\theta) f(t) \quad . \tag{28}$$

The source is located at (1.720, 2.303) km, exactly on the surface. We discretize the model with 23864 triangles, with an average length of 30 m. The time step is set to be 0.468 ms. Part of the mesh is illustrated in Fig. 12, where the pentagram indicates the location of the source.

In Fig. 13, we show the resulting snapshots of the wavefields in the z-direction at T = 0.6 s. The dissipation factors r = 0 and 8 are considered. The Rayleigh wave propagations at the surface can be clearly observed from the figure, showing that the proposed method could be effectively combined with free surface boundary conditions. In addition, we can see that the attenuation of the wave energy is obvious, verifying the attenuation effect in D'Alembert media.

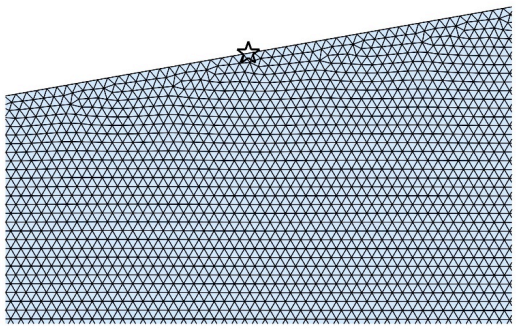

Fig. 12. Part of the mesh for Lamb's model. The pentagram in the figure indicates the location of the source.

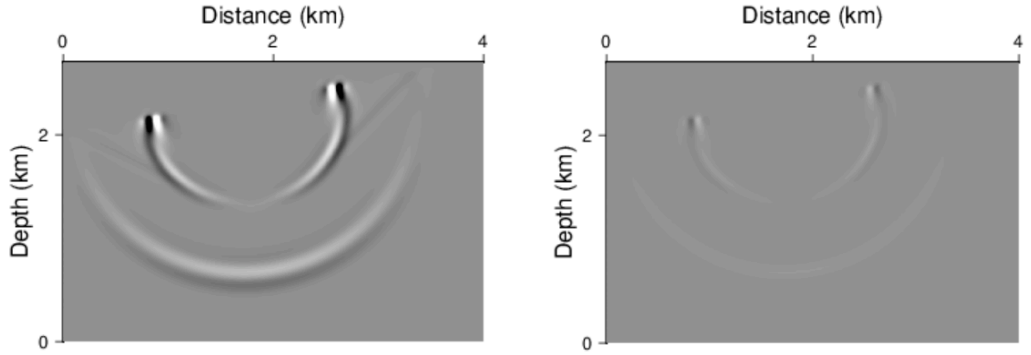

(a) (b)

Fig. 13. Snapshots of the velocity wavefield in the z-direction at T = 0.6 s for Lamb's model. The dissipation factors are: (a) r = 0, (b) r = 8.

Model with surface topography

In the last example, we test the proposed method for dissipative elastic wave propagation with surface topography. The P and SV wave velocities are c_p = 4 km/s and c_s = 2.5 km/s. The density is ρ = 2 g/cm^3. The upper geometry of the model is a curve with a sine function. The Ricker source has a central frequency of f_0 = 15 Hz. The source is loaded in the z-direction, and is located at the surface with coordinates (3.545, 3.894) km. We discretize the model with 66051 triangles with an average length of 30 m. The simulation is carried out for dissipation factors r = 0 and 4. For both cases, the time step is set to 0.5 ms.

Fig. 14 shows the snapshots of the wavefields with the z component at T = 0.8 s for r = 0 and 4. The wave fronts are very clear and the attenuation of the wave energy with r = 4 is obvious. The converging of the wave energy below the curved surface can also be observed. This model shows the validity of the proposed method for modelling wave propagation with surface topography.

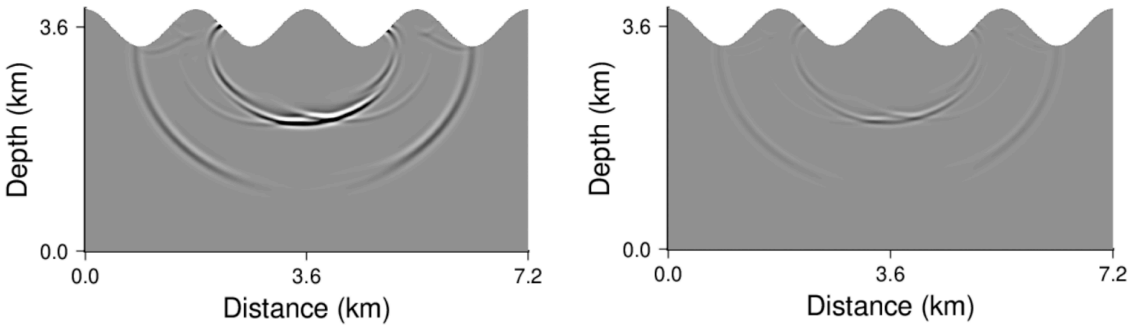

(a) (b)

Fig. 14. Snapshots of the velocity wavefield in the z-direction at $T = 0.8$ s for the model with surface topography. The dissipation factors are taken as (a) $r = 0$ and (b) $r = 4$.

CONCLUSIONS and DISCUSSIONS

In this study, we focus on the DG method for solving seismic wave equations in 2D D'Alembert media. This method employs the flux-based discontinuous Galerkin formulations with the explicit 3rd-order TVD Runge-Kutta method. We analyze the numerical stability conditions, dispersion and dissipation in great detail. For stability conditions, we derive an empirical formula suitable for first-order systems with dissipation. For dispersion and dissipation, we first compare them with the theoretical cases in D'Alembert media, and find that they have good consistency. The analysis shows that both the dispersion and dissipation in D'Alembert media are frequency dependent. At low frequencies, dispersion and dissipation are mainly caused by the viscous term in the seismic equations. As the frequency increases, the dispersion and dissipation caused by the numerical algorithm method gradually increase.

To verify the validity of the proposed method, we have presented several numerical examples. We simulate the dissipative acoustic and elastic wave propagations in D'Alembert media, and study the effects of different dissipation factors on the amplitude of the waves. Under the selected grid conditions, we found that there is almost no visible numerical dispersion, but there exists a significant dissipative effect. We quantitatively analyze the attenuation ratios at the crests and troughs and find that they are close to the theoretical ones, verifying the findings of the dissipation analysis. In addition, we test Lamb's model in D'Alembert media, and observe clear Rayleigh waves at the free surface and their obvious dissipation, demonstrating that our proposed method could be effectively combined with free surface boundary conditions. Finally, we give an example of elastic wave propagation in a model with surface topography, indicating the effectiveness of the method for dealing with complex geometry.

The method can be directly generalized to the 3D case. We are currently considering the 3D DG method in solving dissipative acoustic and elastic equations. But for large-scale 3D simulations, the computational cost is very large, so parallel algorithms will need to be implemented and optimized. These problems will be addressed in future research.

ACKNOWLEDGMENTS

This work was supported by the National Natural Science Foundation of China (Grant Nos. 41974114, 11961020).

REFERENCES

Aki, K. and Richards, P.G., 2002. Quantitative seismology. W.H. Freeman & Co, San Francisco.

Ba, J., Xu, W., Fu, L.Y., Carcione, J.M. and Zhang, L., 2017. Rock anelasticity due to patchy saturation and fabric heterogeneity: A double double-porosity model of wave propagation. J. Geophys. Res.-Solid Earth, 122: 1949-1976.

Cai, W., Zhang, H. and Wang, Y., 2017. Dissipation-preserving spectral element method for damped seismic wave equations. J. Computat. Phys., 350: 260-279.

Carcione, J.M., 1993. Seismic modeling in viscoelastic media. Geophysics, 58: 110-120.

Carcione, J.M. and Cavallini, F., 1994. A rheological model for anelastic anisotropic media with applications to seismic wave propagation. Geophys. J. Internat., 119: 338-348.

Carcione, J.M. and Quiroga-Goode, G., 1995. Some aspects of the physics and numerical modeling of Biot compressional waves. J. Computat. Acoust., 3: 261-280.

Cockburn, B. and Shu, C.W., 1989. TVB Runge-Kutta local projection discontinuous Galerkin finite element method for conservation laws: II. General framework. Mathemat. Computat., 52: 411-435.

de Basabe, J.D., Sen, M.K. and Wheeler, M.F., 2008. The interior penalty discontinuous Galerkin method for elastic wave propagation: grid dispersion. Geophys. J. Internat., 175: 83-93.

de Hoop, A., 1960. A modification of Cagniard's method for solving seismic pulse problems. Appl. Sci. Res. Sec., B 8: 349-356.

de la Puente, J., Dumbser, M., Käser, M. and Igel, H., 2008. Discontinuous Galerkin methods for wave propagation in poroelastic media. Geophysics, 73(5): T77-T97.

Emmerich, H. and Korn, M., 1987. Incorporation of attenuation into time domain computations of seismic wave fields. Geophysics, 52: 1252-1264.

Etienne, V., Chaljub, E., Virieux, J. and Glinsky, N., 2010. An hp-adaptive discontinuous Galerkin finite-element method for 3-D elastic wave modelling. Geophys. J. Internat., 183: 941-962.

Ferroni, A., Antonietti, P. F., Mazzieri, I. and Quarteroni, A., 2017. Dispersion-dissipation analysis of 3-D continuous and discontinuous spectral element methods for the elastodynamics equation. Geophys. J. Internat., 211: 1554-1574.

He, X.J., Yang, D.H. and Wu, H., 2015. A weighted Runge–Kutta discontinuous Galerkin method for wavefield modelling. Geophys. J. Internat., 200: 1389-1410.

Hestholm, S., 1999. Three-dimensional finite-difference viscoelastic wave modelling including surface topography. Geophys. J. Internat., 139: 852-878.

Hu, F.Q., Hussaini, M.Y. and Rasitarinera, P., 1999. An analysis of the discontinuous Galerkin method for wave propagation problems. J. Computat. Phys., 151: 921-946.

Käser, M. and Dumbser, M., 2006. An arbitrary high-order discontinuous Galerkin method for elastic waves on unstructured meshes - I: The two-dimensional isotropic case with external source terms. Geophys. J. Internat., 166: 855-877.

Käser, M., Dumbser, M., de La Puente, J. and Igel, H., 2007. An arbitrary high-order Discontinuous Galerkin method for elastic waves on unstructured meshes-III. Viscoelastic attenuation. Geophys. J. Internat., 168: 224-242.

Kristek, J. and Moczo, P., 2003. Seismic-wave propagation in viscoelastic media with material discontinuities: a 3D fourth-order staggered-grid finite-difference modeling. Bull. Seismol. Soc. Am., 93: 2273-2280.

Lähivaara, T. and Huttunen, T., 2010. A non-uniform basis order for the discontinuous Galerkin method of the 3D dissipative wave equation with perfectly matched layer. J. Computat. Phys., 229: 5144-5160.

Lamb, H., 1904. On the propagation of tremors over the surface of an elastic solid. Phil. Trans. Roy. Soc. London., Ser. A., 203: 1-42.

Lambrecht, L., Lamert, A., Friederich, W. Möller, T. and Boxberg, M.S., 2018. A nodal discontinuous Galerkin approach to 3-D viscoelastic wave propagation in complex geological media. Geophys. J. Internat., 212: 1570-1587.

Li, Q.Y., Yi, D.Y. and Wang, N.C., 2008. Numerical Analysis. Tsinghua University Press (in Chinese).

McLachlan, R.I. and Quispel, G.R.W., 2002. Splitting methods. Acta Numer., 11: 341-434.

Moczo, P. and Kristek, J., 2005. On the rheological models used for time-domain methods of seismic wave propagation. Geophys. Res. Lett., 32: L01306.

Moczo, P., Kristek, J. and Halada, L., 2000. 3D fourth-order staggered-grid finite-difference schemes: Stability and grid dispersion. Bull. Seismol. Soc. Am., 90: 587-603.

Niu, B.H. and Sun C.Y., 2007. Half-Space homogeneous isotropic--viscoelastic medium and seismic wave propagation (in Chinese). Geological Publishing House, Beijing.

Reed, W.H. and Hill, T., 1973. Triangular mesh methods for the neutron transport equation. Los Alamos Scientific Lab., New Mex., U.S.A.

Rivière, B., Shaw, S. and Whiteman, J.R., 2007. Discontinuous Galerkin finite element methods for dynamic linear solid viscoelasticity problems. Numerical Methods for Partial Differential Equations, 23:1149-1166.

Robertsson, J.O., Blanch, J.O. and Symes, W.W., 1994. Viscoelastic finite-difference modeling. Geophysics, 59: 1444-1456.

Sármány, D., Botchev, M.A. and van der Vegt, J.J., 2007. Dispersion and dissipation error in high-order Runge-Kutta discontinuous Galerkin discretisations of the Maxwell equations. J. Scient. Comput., 33: 47-74.

Virieux, J., 1986. P-SV wave propagation in heterogeneous media: velocity-stress finite-difference method. Geophysics, 51: 889-901.

Wang, N., Li, J., Borisov, D., Gharti, H.N., Shen, Y., Zhang, W. and Savage, B., 2019. Modeling three-dimensional wave propagation in anelastic models with surface topography by the optimal strong stability preserving Runge-Kutta method. J. Geophys. Res.: Solid Earth, 124: 890-907.

Wang, N. and Zhou, Y., 2014. A weak dispersion 3D wave field simulation method: A predictor-corrector method of the Implicit Runge-Kutta Scheme. J. Seismic Explor., 23: 431-462.

Wilcox, L.C., Stadler, G., Burstedde, C. and Ghattas, O., 2010. A high-order discontinuous Galerkin method for wave propagation through coupled elastic–acoustic media. J. Computat. Phys., 229: 9373-9396.

Yang, D., He, X., Ma, X., Zhou, Y. and Li, J., 2016. An optimal nearly analytic discrete-weighted Runge-Kutta discontinuous Galerkin hybrid method for acoustic wavefield modeling. Geophysics, 81(5): T251-T263.

Yang, H.Z. and Du, Q.Z., 2003. Finite-element methods for viscoelastic and azimuthally anisotropic media. Acta Phys. Sinica (in Chinese), 52: 2010-2014.